Journal of Sol-Gel Science and Technology (2021) 97:146–154
https://doi.org/10.1007/s10971-020-05419-4

ORIGINAL PAPER: NANO-STRUCTURED MATERIALS (PARTICLES, FIBERS, COLLOIDS, COMPOSITES, ETC.)

Nanocrystalline $SrMnO_3$ perovskite prepared by sol–gel self-combustion method for sensor applications

Corneliu Doroftei[1] · Liviu Leontie[1,2]

Received: 16 June 2020 / Accepted: 22 September 2020 / Published online: 7 October 2020

Abstract

Oxide compound with perovskite-type structure, $SrMnO_3$, was investigated in view of its application as capacitive and/or resistive humidity sensor. The compound presents a porous structure with prevailing open tubular pores systems and it was obtained by sol–gel self-combustion method using polyvinyl alcohol as colloidal medium, followed by heat treatment. Air relative humidity (RH) has a big influence on sensor electric capacity. The best sensitivity as capacitive humidity sensor was found at working frequency of 40 Hz over a wide range of relative humidity (0–98% RH). At this frequency, within the interval 0–98% RH the capacity increases by 1200%, and the resistance decreases by only 18%. The sensor has a good linearity of the log*C* vs. *RH* characteristics. The sensor exhibits very small hysteresis, and a short response time. The investigated material holds promise for humidity monitoring applications, taking into account the low cost, a wide range of relative humidity and a low-contamination impact, as well as for the realization of some electronic components, which requires good stability of resistivity in the presence of environmental humidity factors.

Graphical Abstract

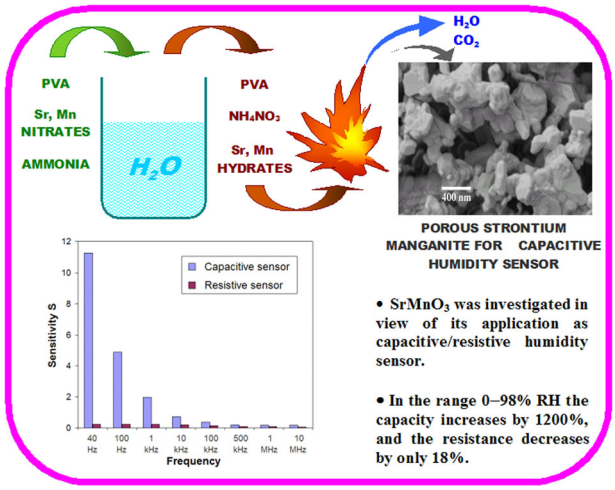

✉ Corneliu Doroftei
docorneliug@gmail.com

[1] Alexandru Ioan Cuza University of Iasi, Institute of Interdisciplinary Research, Integrated Center for Studies in Environmental Science for North-East Region, 11 Carol I Blvd., 7000506 Iasi, Romania

[2] Alexandru Ioan Cuza University of Iasi, Faculty of Physics, 11 Carol I Blvd., 7000506 Iasi, Romania

Keywords Perovskites · $SrMnO_3$ · Sol–gel self-combustion · Structural properties · Electrical properties · Humidity sensors

Highlights

- Sol–gel self-combustion can be successfully used for preparation of $SrMnO_3$.
- In the range 0−98% RH the capacity increases by 1200%, and the resistance decreases by only 18%.
- The investigated material holds promise for capacitive humidity sensors.
- Potential candidate for the achievement of electronic components, which requires good stability of resistivity.

1 Introduction

The measurement and control of humidity is important in many areas, including meteorology, domestic environment, medicine, food production, industry, and agriculture. The development of inexpensive, highly sensitive and selective humidity sensors is still in progress. Desirable characteristics of humidity sensors are high sensitivity over a wide humidity range, quick response time, stability, resistance to contaminants, insignificant dependence on temperature, simple structure, low cost, good thermal and chemical stability [1–4].

The oxide compounds with perovskite-type structure, simple or doped, prepared through various methods, have been investigated as materials with possible applications for electrodes of solid oxide fuel cells [5], metal-air batteries [6], supercapacitors [7–9], gas sensors [10, 11], catalysts [12–16] and resistive humidity sensors [1, 17–25].

However, these types of materials have been less studied with respect to their application potential in capacitive humidity sensors. The adsorption of water vapors is known to enhance the surface electric conductivity and dielectric constant of the oxide compounds [17, 26, 27]. Generally, humidity sensors based on oxide compounds are more chemically and thermally stable than the polymer humidity sensors [18, 26–28]. Resistive sensors are sensitive to the air impurified with gases, which, in the presence of humidity, form electrolytes (sulphur oxides, nitrogen oxides, ammonia, etc.) that can falsify the results of humidity measurement. These shortcomings are partially removed through the utilization of capacitive sensors [18].

Upadhyay and Kavitha [29] realized a study on barium stannate doped with lanthanum ions ($Ba_{1-x}La_xSnO_3$ where $x = 0.0$–0.1) obtained through classical ceramic method, used as resistive and capacitive humidity sensors. The resistance and capacitance of all the samples in the frequency range 20 Hz–1 MHz and relative humidity (RH) range 10–95% have been measured at 31 °C. They noticed that frequency has a bigger influence on sensor capacity, than on sensor resistance. Barium stannate doped with lanthanum ions ($x = 0.1$) has a higher sensitivity to humidity variation. The resistance of the sample doped with lanthanum ions ($x = 0.1$) changes very much, while its capacity changes very little within the RH range 10–95%. At a particular relative humidity, temperature, and frequency (i.e., for RH 10%, temperature 31 °C and frequency 1 kHz), the conductivity of barium stannate increases sharply when dopant (La) concentration increases from 0 to 10 mol%, which is explained in terms of charge compensation mechanism [29, 30].

In the present paper, the oxide compounds with perovskite-type structure, $SrMnO_3$, was synthesized and investigated in view of its application as capacitive and/or resistive humidity sensor. The investigated compound presents a porous structure in which open tubular pores systems prevail, and it was obtained through sol–gel self-combustion method using polyvinyl alcohol as colloidal medium, followed by heat treatment [11, 31–36]. The procedure offers the advantage of producing nanosized, homogeneous and reproducible ceramic samples with high specific surface area and precise stoichiometry [18, 37]. A major advantage of the materials realized through this method is that one obtains porous structures, including open tubular pores systems, favorable to vapors penetration/exhaust into the materials. From this perovskites, one has realized samples/sensor elements in shape of disks with porous silver electrodes on both faces. The samples were investigated with regard to microstructural properties, as well as with sensitivity to humidity within a wide range of relative humidities (0–98% RH), at different frequencies. The active surface of sensing material in contact with the humid air is very large and it is practically situated entirely inside the sensor, being thus protected against solid impurities and aerosols. Therefore, a large amount of contaminants would be necessary for chemical contamination of the entire surface [18].

2 Experimental

Nanocrystalline $SrMnO_3$ perovskite was synthesized by sol–gel self-combustion method using polyvinyl alcohol as colloidal medium. This procedure included the following steps: (a) dissolution of metal nitrates in deionized water; (b) polyvinyl alcohol (10% concentration) addition to nitrate solution to make a colloidal solution; (c) NH_4OH (10%

concentration) addition to increase pH to about 8; a sol of metal hydroxides resulted, according to following equations:

$$Sr(NO_3)_2 + 2 \cdot NH_4OH \rightarrow Sr(OH)_2 + 2 \cdot NH_4NO_3 \quad (1)$$

$$Mn(NO_3)_2 + 2 \cdot NH_4OH \rightarrow Mn(OH)_2 + 2 \cdot NH_4NO_3 \quad (2)$$

(d) stirring at 80 °C to turn the sol of metal hydroxides into gel; (e) drying the gel at 100 °C; (f) self-combustion of the dried gel, according to following equations:

$$C_2H_3OH + 5 \cdot NH_4NO_3 \rightarrow 2 \cdot CO_2 \uparrow + 12 \cdot H_2O \uparrow + 5 \cdot N_2 \uparrow + Q \quad (3)$$

$$2 \cdot Sr(OH)_2 + 2 \cdot Mn(OH)_2 + O_2 \rightarrow Sr_2O_3 + Mn_2O_3 + 4 \cdot H_2O \uparrow \quad (4)$$

$$Sr_2O_3 + Mn_2O_3 \rightarrow 2 \cdot SrMnO_3 \quad (5)$$

(g) calcination at 500 °C for 30 min of the burnt powder to eliminate any organic compounds and residual carbon; (h) cold pressing of powders ($3{\cdot}10^7$ N/m^2) in disk-shaped samples (17 mm diameter, 2 mm thick); (i) heat treatment in air for 10 h at 1000 °C with a heating/cooling rate of 10 °C/min. The migration of ions for the formation of the perovskite structure demands a long treatment time.

In order to investigate the transition temperature in the process of the formation of perovskite-type phases, the powders obtained through self-combustion (without heat treatment) were characterized via thermogravimetric (TG) and differential thermal analysis (DTA) using a Netzsch STA 449 F1 Jupiter instrument, in the temperature range 25–1000 °C at a heating rate of 10 °C/min in static air.

The crystal structure, phase formation and crystallite size of the samples were analyzed by XRD. X-ray diffraction measurements were performed at room temperature using a PANALYTICAL X' PERT PRO MPD diffractometer with CuK$_\alpha$ radiation ($\lambda = 1.54251$ Å). The XRD patterns were recorded between 30° and 80 ° (2θ) at a rate of 2°/min. Crystalline phases were identified by using "Crystallographica" program. The parameters of the unit cell of the crystalline phases were determined with XLAT-Cell Refinement program. The average crystallite size was estimated based on XRD peak broadening, using the Scherrer equation [38, 39]

$$D_x = \frac{0.9\lambda}{\beta \cos\theta} \quad (6)$$

where λ is the wavelength of CuK$_\alpha$ radiation, β is the full width at half maximum of the peak, and θ is the Bragg diffraction angle.

The X-ray density was determined from equation [40]

$$d_x = \frac{M}{Na^3} \quad (7)$$

where M is the molecular weight, N is Avogadro's number, and a is the lattice constant.

A scanning electron microscope (JEOL-200CX) was used to visualize the samples surface morphology. The elemental composition of the grains surface was examined with an Energy Dispersive X-ray Spectrometer (EDX).

The specific surface area (S_{BET}) of the samples was determined from the N_2 adsorption/desorption isotherms at 77 K using the standard Brunauer, Emmet, and Teller (BET) method [41]. Adsorption/desorption isotherms were obtained using Nova-2200 apparatus. The pore size distribution (PSD) curves were obtained using BJH (Barret–Joygner–Halenda) method [41].

In order to realize the sensor elements, porous silver electrodes were applied on both surfaces of the heat-treated disk-shaped samples, using "screen printing" method.

The electric capacitance/resistance of the sample (sensor element) was measured in the frequency range 40 Hz–10 MHz with a precision impedance analyzer (Agilent 4294 A). For the humidity sensing measurements, the sensor element was placed in a thermostatic enclosure at 25 °C and exposed to different values of relative humidity. Relative humidities ranging from 0% to 98% were obtained using as the humidity generation sources saturated salt solutions, such as: LiCl, $K(C_2H_3O_2)$, $MgCl_2$, K_2CO_3, $Mg(NO_3)_2$, $CoCl_2$, NaCl, KCl, K_2SO_4. The dry calcium chloride ($CaCl_2$) was used to obtain dry air (0% RH) [18, 24, 41]. The response time of samples to humidity variation was obtained by monitoring the capacitance variations when the relative humidity varied from 43% to 85% and back.

3 Results and discussion

3.1 Structure and morphology

Figure 1 presents the TG-DTA graphic for the powder obtained as the result of self-combustion reaction. The TG-DTA shows the presence of one exothermic peak at 520–530 °C be, which may due to the reaction of organic compounds combustion and to the residual carbon with total weight loss around 11.2% followed by an endothermic peak at 600 °C that can be assigned to certain crystalline phases of the sample. At higher temperatures one can notice two endothermic peaks, a peak around the value of 930 °C, where one can also remark a decrease of the sample mass, and another peak around 1000 °C, where the mass tends to remain constant, indicating the formation of strontium

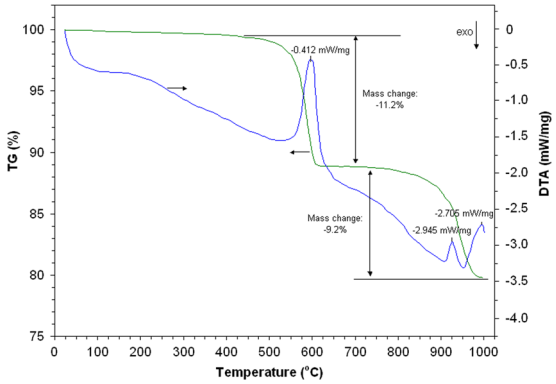

Fig. 1 TG-DTA of synthesizing strontium manganite

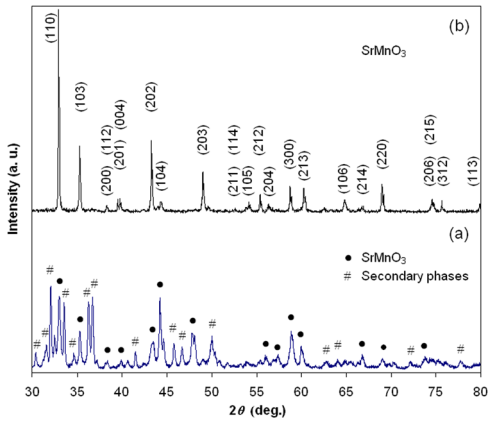

Fig. 2 The XRD patterns of strontium manganite heat treated at 900 °C/20 min (**a**) and heat treated at 1000 °C/10 h (**b**)

manganite with a good crystallinity, which will be also confirmed by the X-ray analyses.

The conventional solid-state reaction method which has been mainly used for the preparation of $SrMnO_3$ manganite needs a temperature of about 1400 °C [42, 43]. Khazaei et al. [44] obtained $SrMnO_3$ perovskite with a good crystallinity, through the citrate method (that uses metals nitrates and citric acid) [45] for a heat treatment of 5 h at 900 °C. In the case of strontium manganite prepared by us through sol–gel self- combustion method, the X-ray diffraction analysis for the samples heat-treated at 900 °C for 20 min (Fig. 2a) indicate the presence of some crystalline phases of $SrMnO_3$, together with numerous secondary phases. This XRD pattern suggests that the annealing temperature must be higher than 900 °C. After sample heat treatment at 1000 °C for 10 h, the X-ray diffractograms (Fig. 2b) indicates the formation of a perovskite-type structure without the presence of secondary phases.

The broadened diffraction peaks indicate that very fine crystallites are present. Referring to the PDF card No. 24–1213, the compound exhibits a hexagonal symmetry (space group P63/mmc). The structural parameters of the sample treated at 1000 °C/10 h, lattice constants, mean

Table 1 The structural parameters of the strontium manganite heat treated at 1000 °C /10 h

Lattice constants (Å)	$a = 5.455$ $c = 9.090$
Average crystallite size D_x (nm)	88.9
X-ray density d_x (g/cm^3)	5.44
Specific surface area S_{BET} (m^2/g)	2.2
Average crystallite size D_{BET} (nm)	500
Total pore volume (cm^3/g)	0.0010

crystal size (D_x) computed from the data of X-ray diffractometries, and X-ray density (d_x) are included in Table 1. The lattice constants (a = 5.455 Å; c = 9.090 Å) are in good agreement with the values reported in literature by other authors [46]. The mean crystallites size (88.9 nm) proves that the perovskites obtained through the sol–gel self-combustion have a nanocrystalline structure.

From the investigation of SEM micrographs, one can state that the studied manganite is characterized by a fine granulation and a porous structure. The grain size varies from 80 nm to 500 nm. The clustering of the particles into mini- or macro-agglomerations with hexagonal facets and irregular sizes is obvious (Fig. 3a). One can remark the presence of large pores distributed along the grain agglomerations, as well as of open tubular pores systems favorable to vapor penetration/exhaust into the sample.

The elemental composition of the sample, heat treated at 1000 °C for 10 h, was examined by the Energy Dispersive X-ray (EDX) spectra. Figure 3b presents the EDX spectrum together with the elemental analysis for this sample. The obtained chemical elemental composition is typical for this perovskite (any foreign element is absent). As can be inferred, the sample composition is similar to that of nominal one, ABO_3, i.e., the A/(A + B) or B/(A + B) ratio is close to 0.5 (where A is Sr at. % and B is Mn at. %.). The method we have used offers the advantage of producing nanosized and homogeneous particles with precise stoichiometry.

Nitrogen adsorption/desorption isotherms at 77 K were used to get information about the specific surface area S_{BET} and pore sizes of the studied manganite. The characteristic isotherms (presented in Fig. 3c for the sample heat treated at 1000 °C for 10 h) correspond to type IV in the IUPAC (International Union of Pure and Applied Chemistry) classification [41] revealing type H3 hysteresis. The inflexion point of isotherms indicates the stage at which monolayer coverage is complete and multilayer adsorptions begin to occur. The pore size distribution graph (PSD) obtained from nitrogen desorption isotherm by BJH method [41] is shown in Fig. 3d. The pore sizes (2–10 nm) fall within mesoporous region (2–50 nm) [41]. One obtains for the specific surface

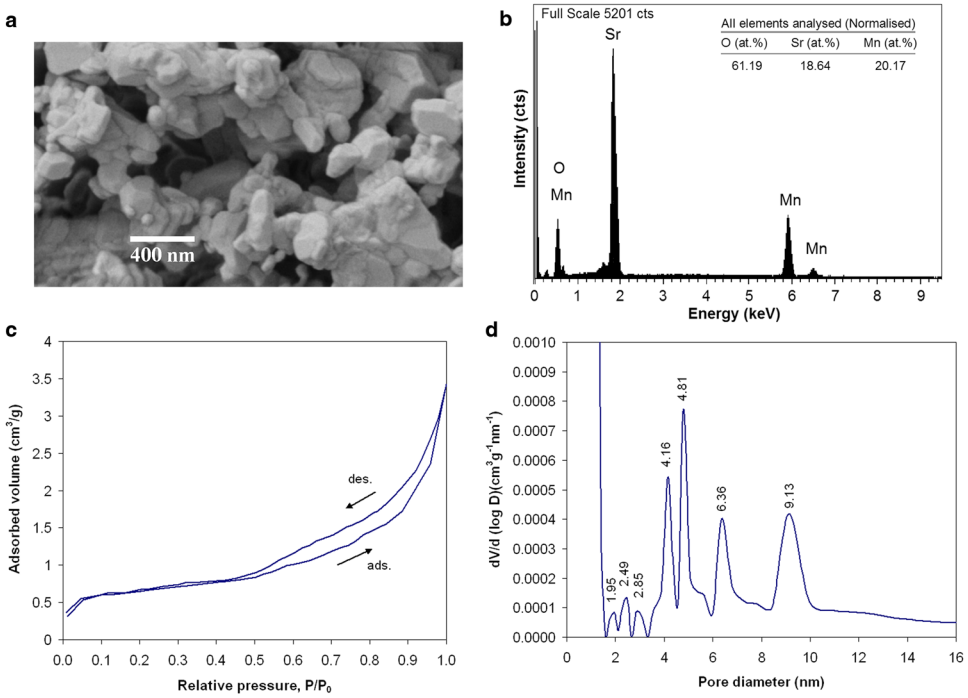

Fig. 3 SEM micrographs (**a**), EDX spectrum with all elements analyzed (**b**), N_2 adsorption/desorption isotherm hysteresis loops (**c**) and pore-size distribution curve (**d**) of the investigated sample after the heat treatment at 1000 °C for 10 h

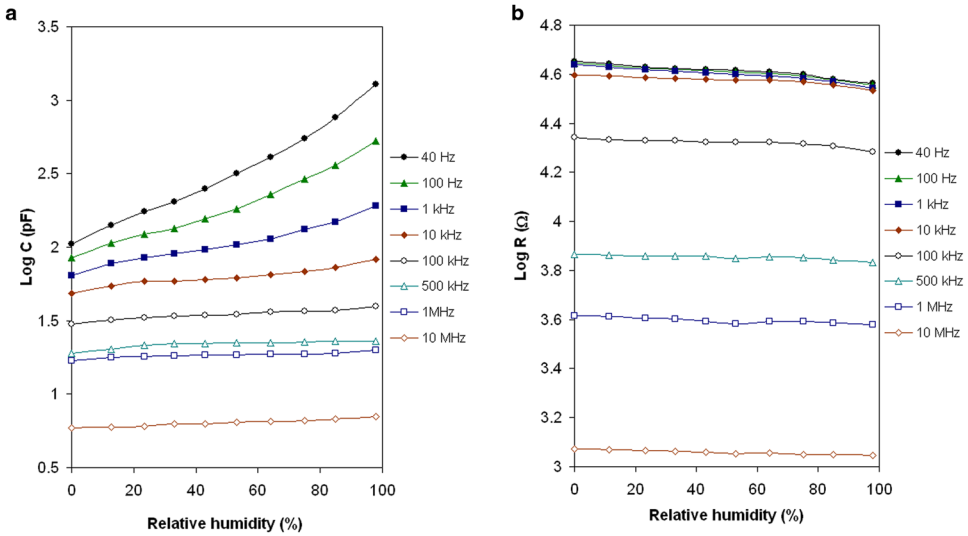

Fig. 4 The capacity (**a**) and resistance (**b**) vs. humidity characteristics for the sensor element at eight measuring frequencies

area (S_{BET}) a value of 2.2 m^2/g and for the pore volume a value of 0.0010 cm^3/g (Table 1).

Using S_{BET} data, the average particle size D_{BET} was calculated with the formula (8) [15, 41] (by assuming that the particles are cubic):

$$D_{BET} = \frac{6}{S_{BET} \cdot d_x} \tag{8}$$

where 6 is the shape factor and d_x is the X-ray density. One can see in Table 1 that D_{BET} is substantially bigger than the X-ray crystallite size D_x. The difference was explained by the concretion of the crystal domains forming the developed network of grain boundaries [18, 47], and attests that the particles are well-crystallized and do not contain defects.

3.2 Sensor properties

The capacitance and resistance of the sensor element at room temperature (25 °C), in the relative humidity range of 0–98%, was measured in the frequency range of 40 Hz–10 MHz. Beyond 10 MHz, water dielectric constant diminishes drastically, and the humidity capacitive sensors are no longer functional. Figure 4a,b presents for

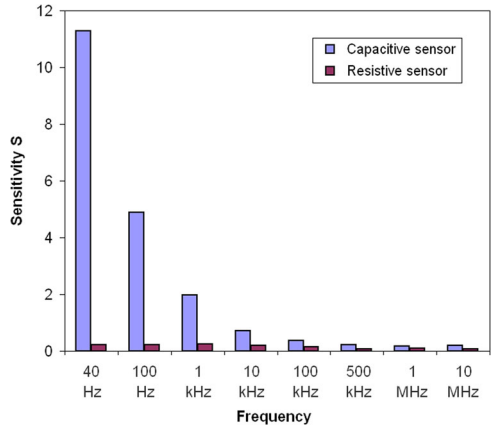

Fig. 5 Bar chart of sensitivity as a function of working frequency, for the investigated range of relative humidity, 0–98%

comparison the log$C$ and logR, respectively vs. RH characteristics for the sensor element at eight working frequencies (40 Hz, 100 Hz, 1 kHz, 10 kHz, 100 kHz, 500 kHz, 1 MHz and 10 MHz). One can notice that the sensor element has characteristics with good linearity at all the frequencies between 0% and 98% RH.

One can notice in Fig. 4a that the slope of Log C vs. RH characteristic increases with the decrease of the working frequency and the highest slope is obtained for the lowest frequency (40 Hz). This can be explained by assimilating the sensor with a network of RC series circuits. Practically, each elementary capacity charges and discharges through an elementary resistance. When increasing the frequency, the capacities charge/discharge less, due to the shorter time, the time constant is being proportional with the RC product. In Fig. 4b, one can notice that up to the frequency of 100 kHz, the Log R vs. RH characteristics are not influenced by frequency.

The humidity sensitivity (S) for a given relative humidity range can be defined as [18, 48]

$$S = \frac{M_{\max}}{M_{\min}} - 1 \tag{9}$$

where M_{max} and M_{min} denote the capacitances (C) or resistances (R) measured for the maximum and minimum values of the RH range, respectively.

Figure 5 presents the humidity sensitivity for different working frequencies, in the relative humidity range of 0–98%. The highest sensitivity value, that capacitive sensor, of 11.27, is obtained for the lowest working frequency (40 Hz), and it decreases down to 0.18 at the working frequency of 10 MHz. As a resistive sensor, the sensitivity value is very low (0.22) at the working frequency of 40 Hz and decreases up to 0.062 at the working frequency of 10 MHz.

When the relative humidity of the environment to which the sensor is exposed has a higher value, the water molecules are absorbed and the sensing material exhibits a leak conduction (γ) [49]. In these conditions the capacitance (C) of the material with leak conduction can be expressed by relation (10) [50, 51]:

$$C = \varepsilon^* C_0 = \left(\varepsilon_r - i\frac{\gamma}{\omega\varepsilon_0}\right) \cdot C_0 \tag{10}$$

where ε^*, C_0 and ε_r are the complex dielectric constant, capacitance and relative dielectric constant of an ideal capacitor, respectively; ω is the angular frequency, γ denotes the conductance and ε_0 is the permittivity of free space. From Eq. (10) it results that the capacitance value decreases with increasing frequency and this decrease becomes much more prominent when RH increases. In addition, γ increases together with RH and as a result, capacitance value increases with rising RH as a function on ω [50].

The mechanism of capacity variation with humidity at a low working frequency can be explained through phenomena of adsorption (chemisorption) and absorption (physisorption) of water molecules and their effect on the variation of capacity of the system consisting of porous material and water [52, 53].

When more layers are adsorbed on the material surface, the next layers will be bound to the inferior layer through only one hydrogen bond, molecules mobility will be larger, and ε_r will increase. When liquid water absorption also occurs, the water molecules are completely mobile, and ε_r has the large value of the bulk water [54]. Condensed water vapors occupy the entire volume of the pores with radius larger than r_K value, according to Kelvin equation [55, 56].

When working frequency increases, energy losses occur, due to ionic conductivity that takes place through hopping transfer of protons between adjacent hydroxyl groups, according to Grotthuss chain reaction (11) [57].

$$H_2O + H_3O^+ \rightarrow H_3O^+ + H_2O \tag{11}$$

These losses result in the decrease of water complex dielectric constant, and implicitly of the slope of log$C$ vs RH curve. The higher the working frequency, more enhanced becomes the slope decrease.

In the case of a humidity resistive sensor, the charge carriers that realize the conduction can be of two types: ionic, in which the sensor element resistivity decreases with the increase of relative humidity due to physisorption and water vapors condensation in capillary, or of electronic type, in which the sensor element conduction depends on semiconductor type, n or p. In the case of electronic conduction, the water molecules chemisorbed on oxide surface play the part of electron-donor [58, 59].

In the case of studied perovskite, its resistivity varies very little with air humidity; therefore, the two conduction mechanisms are not considerably acting. The presence of

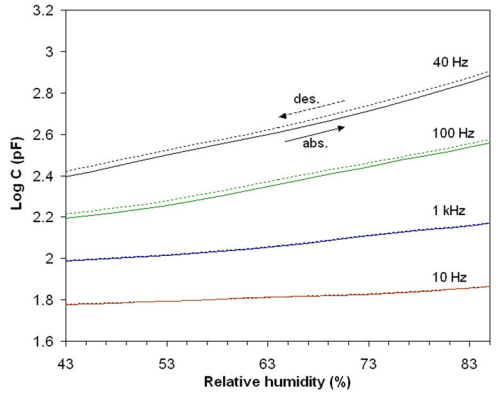

Fig. 6 The hysteresis property of the sensor at 40 Hz, 100 Hz, 1 kHz and 10 kHz

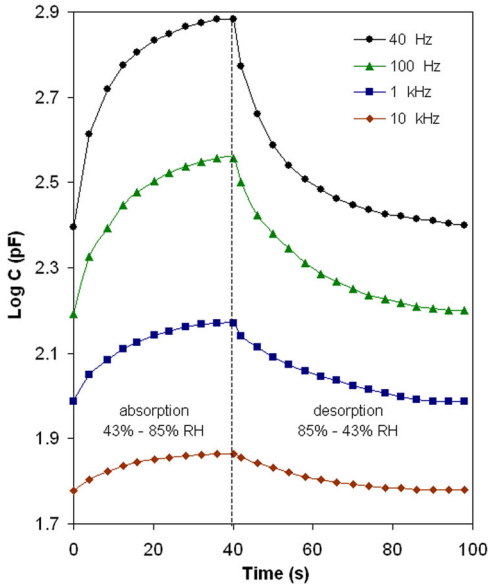

Fig. 7 Humidity time response characteristics for the four working frequencies

water condensed from vapors (without ions) modifies to a very small extent the perovskite conductivity.

The sensor element studied as humidity capacitive sensor exhibits at low frequencies a good reversibility within the investigated humidity range. The maximum difference between the absorbtion and desorbtion curves, in terms of capacitance value is known as hysteresis. High hysteresis values represented a major drawback in practical humidity sensor applications. The sensor was tested at increasing and decreasing RHs and shows very small hysteresis, especially at high RHs. The capacitance hysteresis is of 0.2–2.5% over the entire RH range. When RH decreases, desorption of water molecules does not require much extra energy. This explains the very small hysteresis of the sensor element [26]. Figure 6 presents the absorption and desorption curves (log*C* vs. *RH*) within a narrow humidity range (43–85% RH) and at the working frequencies of 40 Hz, 100 Hz, 1 kHz and 10 kHz.

Taking into account that the studied strontium manganite shows a good sensitivity from the standpoint of a humidity capacitive sensor, one has determined the time of response to humidity variation for different working frequencies. The response time was obtained by monitoring the capacitance variations when the relative humidity changed from 43% to 85% and back.

The humidity response time characteristics at 25 °C for the sensor element within the interval 43–85% RH at the frequencies of 40 Hz, 100 Hz, 1 kHz and 10 kHz are shown in Fig. 7.

The response time required for the response values to attain 90% of its maximum value are of about 30 s for absorption (43–85% RH) and about 40 s in the case of desorption (85–43% RH). We consider these response time values as small for a bulk humidity sensor. The time taken by the sensor element to come back once the water vapors concentration diminished is found to be longer. These results suggest that water vapors adsorption/desorption rate is controlled by the diffusion rate of vapors through the micropores, which in turn depends on the size and distribution of large pores. From the response time characteristics, one can also notice that the response time does not change with working frequency variation.

4 Conclusions

One has investigated the oxide compound with perovskite-type structure, $SrMnO_3$, in view of its application as humidity capacitive or resistive sensor. It was synthesized by sol–gel self-combustion method using polyvinyl alcohol as colloidal medium, followed by heat treatment for 10 h at 1000 °C. The samples exhibit a good crystallinity and a porous granular structure with average crystallite size 88.9 nm, specific surface area of 2.20 m^2/g and total pore volume of 0.0010 cm^3/g.

The electric capacitance/resistance of the sample (sensor element) was measured within the range of 0–98% RH and at various frequencies between 40 Hz and 10 MHz. Relative air humidity (RH) influences to a much bigger extent the sensor electric capacity, as compared to its electric resistance. The electric capacity increases with increasing RH at all measuring frequencies and decreases with increasing working frequency. The best sensitivity as capacitive humidity sensor over a wide range of relative humidity, 0–98% RH was found at working frequency of 40 Hz. At this frequency, for humidity range 0−98% RH, the sensitivity of the capacitive sensor is of 11.27, while the sensitivity of resistive sensor is only of 0.22. The sensor element has characteristics (Log C and Log R vs. RH) with good linearity at all the frequencies between 0% and 98% RH;

moreover, up to the frequency of 100 kHz, the characteristics Log R vs. RH are not influenced by the frequency.

The capacitive sensor exhibits very small hysteresis (2.5%), and a short response time (30 s) at working frequency of 40 Hz. The investigated material holds promise for humidity monitoring applications, taking into account the low cost, a wide range of relative humidity and a low-contamination impact, as well as for the realization of some electronic components that require good stability of resistivity in the presence of environmental humidity factors.

Compliance with ethical standards

Conflict of interest The authors declare that they have no conflict of interest.

Publisher's note Springer Nature remains neutral with regard to jurisdictional claims in published maps and institutional affiliations.

References

1. Josephine BA, Manikandan A, Teresita VM, Antony SA (2016) Fundamental study of LaMgxCr1−xO3−δ perovskites nano-photocatalysts: Sol-gel synthesis, characterization and humidity sensing. Korean J Chem Eng 33:1590–1598
2. Chen Z, Lu C (2005) Humidity sensors: a review of materials and mechanisms. Sens Lett 3:274–295
3. Vijaya JJ, John Kennedy L, Meenakshisundaram A, Sekaran G, Nagaraja KS (2007) Humidity sensing characteristics of sol-gel derived Sr(II)-added ZnAl2O4 composites. Sens Actuators B Chem 127:619–624
4. Zou H, Zhang Y, Duan Z, Tong Y, Peng J, Zheng X (2018) Humidity sensing properties of LnFeO3 nanofibers synthesized by electrospinning (Ln = Sm, Nd, La). Mater Res Express 5:015022
5. Qi T, Levchenko SV, Bennett JW, Grinberg I, Rappe AM (2009) New prospects for high performance SONAR, chemical sensor and communication device materials, HPCMP-UGC 2009: Proceedings of the 2009 DoD high performance computing modernization program users group, IEEE 1:197–204
6. Shimizu Y, Uemura K, Matsuda H, Miura N, Yamazoe N (1990) Bi-functional oxygen electrode using large surface area La1−xCaxCoO3 for rechargeable metal-air battery. J Electrochem Soc 137:3430–3433
7. Lang X, Mo H, Hu X, Tian H (2017) Supercapacitor performance of perovskite La1−xSrxMnO3. Dalton Transactions 46:13720–13730
8. Shi W, Ding R, Li X, Xu Q, Ying D, Huang Y, Liu E (2017) Bimetallic Co-Mn perovskite fluorides as highly-stable electrode materials for supercapacitors. Chem Eur J 23:15305–15311
9. Ding R, Li XD, Shi W, Xu QL, Han XL, Zhou Y, Hong WF, Liu EH (2017) Perovskite KNi0.8Co0.2F3 nanocrystals for supercapacitors. J Mater Chem A 5:17822–17827
10. Hunter GW, Xu JC, Evans LJ, Vander Wal RL, Gordon M (2006) Chemical sensors based on metal oxide nanostructures, applications. Solid-State Ionic Devices 9:199–209
11. Doroftei C, Popa PD, Iacomi F (2013) Selectivity between methanol and ethanol gas of La-Pb-Fe-O perovskite synthesized by novel method. Sens Actuators A 190:176–180
12. Shaterian M, Enhessari M, Rabbani D, Asghari M (2014) Synthesis, characterization and photocatalytic activity of LaMnO3 nanoparticles. Appl Surf Sci 318:213–217
13. Alifanti M, Kirchnerova J, Delmon B (2003) Effect of substitution by cerium on the activity of LaMnO3 perovskite in methane combustion. Appl Catal A 245:231–244
14. Tian T, Wang W, Zhan M, Chen C (2010) Catalytic partial oxidation of methane over SrTiO3 with oxygen-permeable membrane reactor. Catal Commun 11:624–628
15. Rezlescu N, Rezlescu E, Popa PD, Doroftei C, Ignat M (2013) Nanostructured GdAlO3 perovskite, a new possible catalyst for combustion of volatile organic compounds. J Mater Sci 48:4297–4304
16. Rezlescu N, Rezlescu E, Popa PD, Doroftei C, Ignat M (2015) Some nanograined ferrites and perovskites for catalytic combustion of acetone at low temperature. Ceram Int 41:4430–4437
17. Aria H, Ezeki S, Shimizu Y, Shippo O, Seiyama T (1983) Semiconductive humidity sensor of perovskite-type oxides. Anal Chem Symp Ser Chem Sens 17:393–398
18. Leontie L, Doroftei C, Carlescu A (2018) Nanocrystalline iron manganite prepared by sol–gel self-combustion method for sensor applications. Appl Phys A 124:750
19. Lucaszewicz JP (1991) Diode-type humidity sensor using perovskite-type oxides operable at room temperature. Sens Actuators B 4:227–232
20. Wang Z, Chen C, Zhang T, Guo H, Zou B, Wang R, Wu F (2007) Humidity sensitive properties of K+ - doped nanocrystalline LaCo0.3Fe0.7O3. Sens Actuators B 126:678–683
21. Ansari ZA, Ko TG, J.Oh JH (2004) Humidity sensing behavior of thick films of strontium-doped lead-zirconium-titanate. Surf. Coatings Technol 179:182–187
22. Yeh YC, Tseng TY (1989) Analysis of the d.c. and a.c. properties of K2O-doped porous Ba0.5Sr0.5TiO3 ceramic humidity sensor. J Mater Sci 24:2739–2745
23. Holc J, Slunecko J, Hrovat M (1995) Temperature characteristics of electrical properties of (Ba,Sr)TiO3 thick film humidity sensors. Sens. Actuators B 26–27:99–102
24. Doroftei C, Popa PD, Iacomi F (2012) Study of the influence of nickel ions substitutes in barium stannates used as humidity resistive sensors. Sens Actuators A 173:24–29
25. Ke S, Huang H, Fan H, Chan HLW, Zhou LM (2008) Structural and electric properties of barium strontium titanate based ceramic composite as a humidity sensor. Solid State Ion 179:1632–1635
26. Wang Y, Park S, Yeow JTW, Langner A, Müller F (2010) A capacitive humidity sensor based on ordered macroporous silicon with thin film surface coating. Sens Actuators B 149:136–142
27. Traversa E (1995) Ceramic sensors for humidity detection: the State-of-the-art and future developments. Sens Actuators B 23:135–156
28. Rezlescu N, Rezlescu E, Doroftei C, Popa PD (2005) Study of some Mg-based ferrites as humidity sensors. J Phys: Conf Series 15:296–299
29. Upadhyay S, Kavitha P (2007) Lanthanum doped stannate for humidity sensor. Mat Letters 61:1912–1915
30. Madhan K, Murugaraj R (2020) Structural, electrical, and weak ferromagnetic-to-antiferromagnetic nature of Ni and La co-doped BaTiO3 by sol-gel combustion route. J Sol-Gel Sci Technol 95:11–21
31. Doroftei C, Popa PD, Iacomi F, Leontie L (2014) The influence of Zn2+ ions on the microstructure, electrical and gas sensing properties of La0.8Pb0.2FeO3 perovskite. Sens Actuators B 191:239–245
32. Doroftei C, Leontie L (2017) Synthesis and characterization of some nanostructured composite oxides for low temperature catalytic combustion of dilute propane. RSC Adv 7:27863–27871
33. Rezlescu N, Doroftei C, Rezlescu E, Popa PD (2006) Fine grained erbium doped strontium hexaferrite. Phys Stat Sol A 203:3844–3851

34. Doroftei C, Popa PD, Rezlescu N (2010) The influence of the heat treatment on the humidity sensitivity of magnesium nanoferrite. J Optoelectron Adv Mater 12:881–884
35. Doroftei C, Leontie L (2019) The influence of Sc3+ ions on the microstructure, electrical, and gas-sensing properties of Ni-Co-Sc ferrite. J Sol-Gel Sci Techn 91:654–663
36. Doroftei C, Leontie L, Popa A (2017) The study on nanogranular system manganites La-Pb-Ca-Mn-O which exhibits a large magnetoresistance near room temperature. J Mater Sci: Mater Electron 28:12891–12899
37. Rezlescu N, Popa PD, Rezlescu E, Doroftei C (2008) Microstructure characteristics of some polycrystalline oxide compounds prepared by sol-gel-selfcombustion way for gas sensor applications. Rom J Phys 53:545–555
38. Leontie L, Doroftei C (2017) Nanostructured spinel ferrites for catalytic combustion of gasoline vapors. Catal Lett 147: 2542–2548
39. Klung H, Alexander L (1962) X-ray diffraction procedures. Wiley, New York
40. Habibi MH, Mosavi V (2017) Urea combustion synthesis of nanostructure bimetallic perovskite FeMnO3 and mixed monometallic iron manganese oxides: effects of preparation parameters on structural, opto-electronic and photocatalytic activity for photodegradation of Basic Blue 12. J Mater Sci: Mater Electron 28:8473–8479
41. Lowell S, Shields JE, Thomas MA, Thommes M (2004) Characterization of porous solids and powders: surface area, pore size and density. Kluwer Academic Publishers, Dordrecht (Boston, London)
42. Sammes NM, Philipps MB (1993) The synthesis of La1-xSrxMnO3 at different sintering temperatures. J Mater Sci Lett 12:829–830
43. Zhu D, Zhu H, Zhang Y (2002) Hydrothermal synthesis of La0.5Ba0.5MnO3 nanowires. Appl Phys Lett 80:1634–1636
44. Khazaei M, Malekzadeh A, Amini F, Mortazavi Y, Khodadadi A (2010) Effect of citric acid concentration as emulsifier on perovskite phase formation of nano-sized SrMnO3 and SrCoO3 samples. Cryst Res Technol 45:1064–1068
45. Abadian L, Malekzadeh A, Khodadadi A, Mortazavi Y (2008) Effects of excess cobalt oxide nanocrystallites on LaCoO3 catalyst on lowering the light off temperature of CO and hydrocarbons oxidation. Iran J Chem Chem Eng 27:71–77
46. Søndenå R, Ravindran P, Stølen S (2006) Electronic structure and magnetic properties of cubic and hexagonal SrMnO3. Phys Rev B 74:144102
47. Ivanov DV, Pinaeva LG, Sadovskaya EM, Isupova LA (2011) Influence of the mobility of oxygen on the reactivity of La1—xSrxMnO3 perovskites in methane oxidation. Kinetics Catal 52:401–408
48. Tripathy A, Pramanik S, Cho J, Santhosh J, Osman NAA (2014) Role of morphological structure, doping, and coating of different materials in the sensing characteristics of humidity sensors. Sens 14:16343–16422
49. Wang J, Wang XH, Wang XD (2005) Study on dielectric properties of humidity sensing nanometer materials. Sens Actuators B 108:445–449
50. Tripathy A, Pramanik S, Manna A, Bhuyan S, Shah NFA, Radzi Z, N.A.A. Osman NAA (2016) Design and development for capacitive humidity sensor applications of lead-free Ca, Mg, Fe, Ti - Oxides-based electro-ceramics with improved sensing properties via physisorption. Sens 16:1135–1152
51. Bi H, Yin K, Xie X, Ji J, Wan S, Sun L, Terrones M, Dresselhaus MS (2013) Ultrahigh humidity sensitivity of graphene oxide. Sci Rep 3:2714–2720
52. Yadav BC, Srivastava R, Dwivedi CD (2008) Synthesis and characterization of ZnO-TiO2 nanocomposite and its application as a humidity sensor. Philos Mag 88:1113–1124
53. Das J, Hossain SM, Chahraborty S (2001) Role of parasitic in humidity sensing by porous silicon. Sens Actuators A 94:44–52
54. Wang Z, Shi L, Wu F, Yuan S, Zhao Y, Zhang M (2011) The sol-gel template synthesis of porous TiO2 for a high performance humidity sensor. Nanotech 22:275502–275509
55. Adamson AW, Gast AP (1997) Physical chemistry of surfaces, 6th ed. Wiley-Blackwell, USA
56. Gregg SJ, Sing KSW (1982) Adsorption, surface area and porosity, second ed. Academic Press, New York
57. Agmon N (1995) The Grotthuss mechanism. Chem Phys Lett 244:456–462
58. Arai H, Ezaki S, Shimizu Y, Shippo O (1983) Semiconductive humidity sensor of perovskite-type oxides. Proc Int Meeting on Chemical Sensors, Fukuoka, Sept. 19–22:393–398
59. Taguchi H, Takahashi Y, Matsumoto C (1980) The effect of water adsorption on (La1-xSrx)MnO3 (0.1≤x≤0.5). Yogyo Kyokai Shi 88:566–570